Lateral load response of a dry-joint masonry arch subject to vertical support displacements by rigid block analysis

Meccanica (2025) 60:2001–2018
https://doi.org/10.1007/s11012-024-01927-7

RESEARCH

Lateral load response of a dry-joint masonry arch subject to vertical support displacements by rigid block analysis

Chiara Ferrero · Francesco P. A. Portioli · Chiara Calderini

Received: 20 July 2024 / Accepted: 7 December 2024 / Published online: 11 January 2025

Abstract Masonry arches play a crucial role in the seismic response of historic masonry buildings. Although masonry arches are often subjected to large support displacements that alter and deform their geometries over time, their response to seismic actions is generally analysed using idealized, perfect geometries. This paper aims to assess the effect of large support displacements on the response of masonry arches to lateral loads. To this end, a small-scale segmental dry-joint masonry arch subjected to the vertical displacement of one support was investigated. Using a rigid block modelling approach recently proposed in the literature, the arch was modelled as an assemblage of rigid voussoirs connected by no-tension frictional contact interfaces. The response of the arch to lateral loads, applied in one direction, and to vertical support displacements was assessed through nonlinear static analyses. To evaluate the effect of support displacements, lateral loads were applied to a series of deformed arch geometries resulting from the application of increasing values of the imposed vertical displacement. The results of the numerical analyses provided new insights into how support displacements affect the lateral load response of masonry arches, showing that they may significantly reduce both the horizontal action triggering collapse and the ultimate displacement capacity.

Keywords Dry-joint masonry arches · Large support displacements · Lateral load response · Rigid block modelling · Limit analysis

C. Ferrero · C. Calderini
Department of Civil, Chemical and Environmental Engineering, University of Genoa, Via Montallegro 1, 16145 Genoa, Italy
e-mail: chiara.ferrero@edu.unige.it

C. Calderini
e-mail: chiara.calderini@unige.it

F. P. A. Portioli (✉)
Department of Structures for Engineering and Architecture, University of Naples Federico II, Via Forno Vecchio 36, 80134 Naples, Italy
e-mail: fportiol@unina.it

1 Introduction

Arches have been used since ancient times to cover large spans in masonry structures, with the result that today they are one of the most common structural elements in historic masonry buildings. Traditionally, masonry structures were designed primarily to resist vertical gravity loads, with little consideration for their ability to withstand horizontal loads. Consequently, historic masonry buildings are highly vulnerable to seismic actions, as demonstrated by the extensive damage caused by earthquakes worldwide (e.g., [1–7]). To address this vulnerability, the scientific community is actively working to improve the seismic performance of historic masonry buildings. This effort involves an increasing number of studies aimed at developing a deeper understanding of the seismic

behaviour of masonry structural elements, such as arches.

In recent decades, extensive knowledge has been gained about the seismic response of masonry arches. The observation and analysis of earthquake damage has led to the identification of the collapse mechanisms triggered by seismic actions ([8, 9]). Furthermore, several research works provided valuable insights into the lateral load-carrying capacity of arches and arch-pillar systems (e.g., [10–22]).

To date, most research on arches subjected to horizontal actions has focused on idealized arch geometries—primarily circular, pointed and segmental—derived from perfect, symmetric arcs of circumference (e.g., [10–14, 16–18, 21, 22]). However, these idealized geometries may differ significantly from the actual ones observed in historic masonry buildings, where arches often exhibit large deformations (Fig. 1).

Several factors contribute to the large deformations observed in masonry arches, including gravity loading, construction processes, long-term creep, material degradation, and external actions, such as earthquakes, landslides, foundation settlements, and point loads transmitted by adjacent structures (e.g., roofing systems) [25]. Many of these factors can act for years or decades, resulting in gradual, progressive deformations that can pose a threat to the stability and structural safety of masonry arches [26].

Among the causes of the large deformations exhibited by masonry arches, support displacements play a primary role. Support displacements occur very frequently and can originated from various causes, such as foundation settlements, subsidence, earthquakes, landslides, and soil degradation. Generally, they increase progressively over time, gradually altering the geometry of masonry arches [26]. To provide an example, the combination of vertical and horizontal support displacements produced by slow-moving landslides was recently found to cause large deformations and extensive damage in the arches of historic masonry churches located in the Liguria region, Italy (see [23, 27]). Examples of these deformations are shown in Fig. 1.

In recent years, the response of masonry arches to large support displacements has been extensively studied (e.g., [26, 28–43]). However, to the authors' knowledge, only a limited number of works ([15, 24, 44, 45]) have explored how support displacements and large deformations affect the behaviour of these structural elements. Among these works, only two have specifically investigated the response of masonry arches to lateral loads. In [15], the behaviour of a buttressed arch under lateral loads and inclined support displacements was analysed, whereas [45] focused on the seismic response of a stand-alone arch subjected to horizontal support movements.

Additionally, two other studies have addressed the effects of deformed geometry and support displacements on the response of masonry arches to vertical loads. In [24], the structural safety of a brick masonry arch under vertical point loads transmitted by the roof was assessed considering both the deformed and undeformed geometries of the arch. In [44], the authors evaluated the capacity of a circular arch subjected to horizontal support displacements to withstand vertical point loads applied at the extrados at mid span.

This paper aims to provide new insights into the effect of large support displacements on the response of masonry arches to lateral loads. To achieve this, the behaviour of a small-scale segmental dry-joint masonry arch subjected to vertical displacements at the right support was investigated. The arch was

a) b)

Fig. 1 Large deformations of masonry arches in historic masonry buildings: **a** Sant'Olcese church in Sant'Olcese, Italy [23], **b** Nostra Signora della Bastia sanctuary in Bastia, Italy [24]

analysed using an optimization-based 2D rigid block modelling approach recently proposed in the literature (see [15, 46]). Following this approach, the arch was modelled as an assemblage of rigid voussoirs connected by no-tension frictional contact interfaces that exhibit rigid behaviour.

The response of the arch to lateral loads, simulating seismic actions in one direction, and to support displacements was assessed through nonlinear static analyses. First, a preliminary pushdown analysis was performed to evaluate the arch's behaviour when subjected to the vertical displacement of the right support. Subsequently, sequential pushdown-pushover analyses were conducted. In these analyses, lateral loads were applied to a series of deformed geometries of the arch, resulting from the application of increasing values of vertical support displacement. For comparison, an additional sequential analysis was performed considering the arch in its undeformed configuration, with no vertical displacement imposed at the right support. In the sequential pushdown-pushover analyses, both elastic (with high stiffness values) and rigid contact formulations were used for the interfaces.

The main novelty of this work consists of performing sequential pushdown-pushover analyses to thoroughly investigate the evolution of the arch's behaviour from the application of support displacements to the ultimate conditions under lateral loads. Furthermore, to the authors' knowledge, this research is the first to assess how the magnitude of vertical support displacements affects the arch's response to lateral loads. New insights are provided regarding activation of collapse mechanisms, evolution of the hinge configuration, response curves, and ultimate displacement capacity. This work extends and fully reinterprets preliminary results presented in [47].

The paper is organized as follows. Section 2 presents the numerical case study, illustrating the geometry (Sect. 2.1), modelling approach (Sect. 2.2), material properties (Sect. 2.3), and numerical solution procedures (Sect. 2.4). Section 3 discusses the numerical simulations, starting with an overview in Sect. 3.1. Subsequently, Sect. 3.2 presents the results of the preliminary pushdown analysis under vertical support displacements, while Sects. 3.3 and 3.4 discuss the outcomes of the sequential pushdown-pushover analyses. Finally, Sect. 4 draws conclusions and outlines future work.

2 Numerical case study

2.1 Geometry

The case study analysed in this paper is a small-scale (1:10) segmental dry-joint masonry arch supported by two piers (Fig. 2). The arch has the same geometry as the physical arch tested experimentally to collapse due to vertical, horizontal, and inclined displacements of the right support in [40, 48]. As described in [39], the arch geometry is representative of the standard cross-section of barrel vaults typically used as ceiling in the main nave of historic masonry churches.

As shown in Fig. 2, the arch has an angle of embrace of 125°, a span length of 533 mm, a rise of 162 mm and a radial thickness of 24 mm. It is composed of 55 voussoirs with dimensions $24 \times 12 \times 120$ mm and slightly trapezoidal shape to compensate for the lack of mortar joints. The piers, differing in geometry from those of the experimental mock-up tested in [40, 48], solely provide support for the arch and do not influence collapse mechanisms [49].

2.2 Modelling approach

The response of the arch was analysed using the 2D rigid block modelling approach presented in [15]. According to this approach, arches are modelled as assemblages of rigid blocks that interact at no-tension, frictional contact interfaces. The interfaces are characterized by a four point-based contact model that concentrates internal forces at the vertices.

The numerical model of the arch (Fig. 3) was created using DynABlock_2D [46], a standalone MATLAB application based on the aforementioned modelling approach. This application is suitable for limit equilibrium analysis, nonlinear static

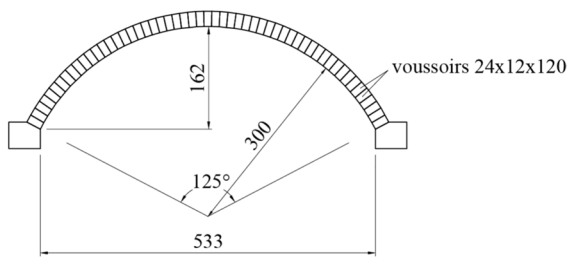

Fig. 2 Geometry of the arch under study (dimensions in mm)

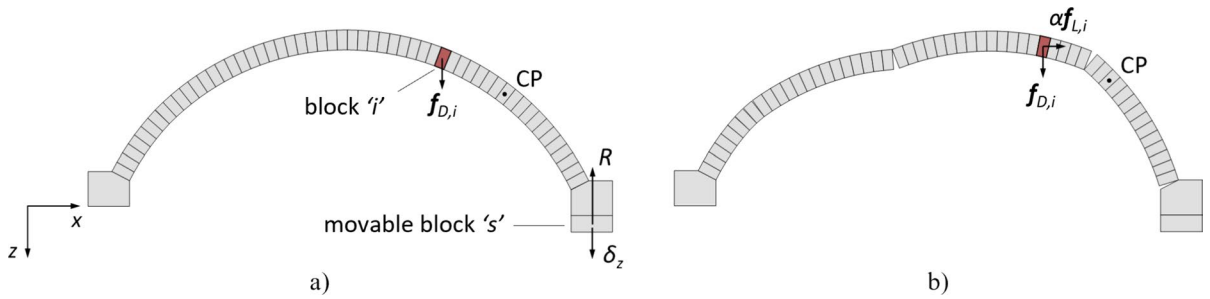

Fig. 3 Rigid block model and loading configurations: **a** pushdown analysis; **b** pushover analysis with imposed support displacement. The control point CP used in the numerical simulations is also indicated

analysis and nonlinear dynamic analysis of dry-joint masonry structures subjected to support displacements and seismic actions. An enhanced version of DynABlock_2D was used in this work, integrating a post-processing subroutine specific to masonry arches. This feature enables plotting of thrust lines and identification of hinge locations.

Various types of nonlinear static analyses were performed on the arch, including pushdown analyses under imposed support displacements and sequential pushdown-pushover analyses (also referred to as sequential analyses). In the sequential analyses, a pushdown analysis (under support displacements) and a pushover analysis (under lateral loads) were performed sequentially, and lateral loads were applied to a deformed arch geometry resulting from the application of support displacements. The pushover analyses aimed to: (i) evaluate the initial behaviour of the arch before the activation of the collapse mechanism under lateral loads, and (ii) investigate the evolution of the collapse mechanism until the ultimate condition, where the arch reaches its ultimate displacement capacity and can no longer withstand lateral loads. A control point (CP), corresponding to the centroid of the 12th voussoir from the right support (see Fig. 3), was used in the numerical simulations to track the arch's horizontal displacements.

Depending on the type of analysis, different boundary conditions and forces acting on the blocks were considered. In the pushdown analyses (Fig. 3a), a movable block, *s*, associated with a single degree of freedom, was added at the right support to impose vertical displacements δ_z. Each voussoir of the arch was subjected to a known dead load $f_{D,i}$, proportional to its self-weight.

In the pushover analyses (Fig. 3b), both the supports of the arch were fixed. Each block of the arch was subjected to a known dead load $f_{D,i}$, proportional to its self-weight, as wells as a lateral load $\alpha f_{L,i} = \alpha f_{D,i}$, which was proportional to the dead load through a load multiplier, α. The load multiplier at the activation of the collapse mechanism was referred to as the initial load multiplier, α_0. As shown in Fig. 3b, a uniform distribution of lateral loads, directed from the left to the right support of the arch, was applied over the blocks to represent seismic actions in that direction.

The 2D rigid block modelling approach used in this work allows for either elastic or rigid contact formulations [15]. In accordance with [15], different contact formulations and corresponding solution procedures were employed in this work for pushover analyses. Before the activation of the collapse mechanism under lateral loads ($\alpha = \alpha_0$), an elastic contact formulation was used, and a load-controlled analysis was performed, where the known load multiplier α was gradually increased from zero to α_0.

Once the collapse mechanism was triggered, a rigid contact formulation was adopted. In this case, a sequential displacement-controlled solution procedure was implemented to analyse the evolution of the rigid body mechanism and the effects of large displacements on the load multiplier α. The horizontal displacement applied at the control point (CP in Fig. 3) was incrementally increased until the arch could no longer withstand lateral loads ($\alpha = 0$). The load multiplier α was treated as an unknown, dependent on the deformed geometric configuration of the arch.

2.3 Material properties

The numerical modelling approach adopted in this work requires only a few material properties as input: the unit weight and friction coefficient of the blocks, as well as the normal contact stiffness (k_n) of the interfaces when an elastic contact formulation is used.

For the arch under study, the unit weight of the blocks was set to 16.1 kN/m^3, and the friction coefficient was set to 0.7, consistent with the values measured experimentally for the physical mockup (see [40]).

The interfaces were treated as rigid, regardless of the contact formulation adopted. Accordingly, when an elastic contact formulation was employed, the normal contact stiffness was set to a high value ($k_n = 1000$ N/mm^3) to ensure rigid behaviour. This stiffness value was determined based on a sensitivity analysis in which the arch's behaviour was investigated under vertical displacement at the right support.

In this analysis, the joints between the voussoirs were discretized into 16 contact interfaces, and the normal contact stiffness k_n was varied from 0.1 to 10,000 N/mm^3. To identify the value of k_n for which the interfaces behaved as rigid, the effect of k_n on the arch's response was evaluated in terms of ultimate collapse displacement, hinge position, and reaction curves. Additionally, the results from the elastic contact formulation were compared to those from a rigid contact formulation, demonstrating that the interfaces exhibited rigid behaviour for $k_n = 1000$ N/mm^3. Further evidence of this rigid behaviour is provided in Sect. 3.3.

2.4 Numerical solution procedures

Following [15], the numerical problems associated with the response of the arch to support displacements and lateral loads were formulated in terms of optimization problems. At each displacement or load increment, a force-based optimization problem and its dual displacement-based problem were solved.

In the pushover analyses with a rigid contact formulation, the force-based optimization problem used to derive the load multiplier α and the contact forces at each increment was expressed as follows:

$$\begin{aligned} &\max \ \alpha\gamma - \boldsymbol{g}_0^{\mathrm{T}}\boldsymbol{c} \\ &\text{s.t.} \ \ \boldsymbol{A}_0\boldsymbol{c} = \boldsymbol{f_D} + \alpha\boldsymbol{f_L} \\ &\qquad \boldsymbol{Y}^{\mathrm{T}}\boldsymbol{c} \le 0 \end{aligned} \tag{1}$$

where:

- γ is the scaling factor associated to the work done by lateral loads ($\boldsymbol{f}_L^{\mathrm{T}}\boldsymbol{\Delta x} = \gamma$), where Δx is the vector collecting the displacements Δx_i, Δz_i, and $\Delta\omega_i$ of the rigid blocks i, referenced to the centroids of each block;
- $\boldsymbol{g}_0$ is the (2c × 1) vector collecting contact gaps in subvectors $\boldsymbol{g}_{0,k}{}^{\mathrm{T}} = (g_{0,k}\ 0)$, where c is the number of contact points;
- $\boldsymbol{c}$ is the vector of the unknown normal and tangential contact forces n_k and t_k acting at contact points of the interfaces k;
- $\boldsymbol{A}_0$ is the equilibrium matrix at configuration $\boldsymbol{x}_0$;
- $\boldsymbol{Y}^{\mathrm{T}}$ is the matrix of failure conditions;
- $\boldsymbol{f_D}$ is the vector of dead loads and includes the subvectors $\boldsymbol{f}_{\boldsymbol{D},\boldsymbol{i}} = \begin{bmatrix} 0 & \rho V_i & 0 \end{bmatrix}^{\mathrm{T}}$, where ρ and V_i are

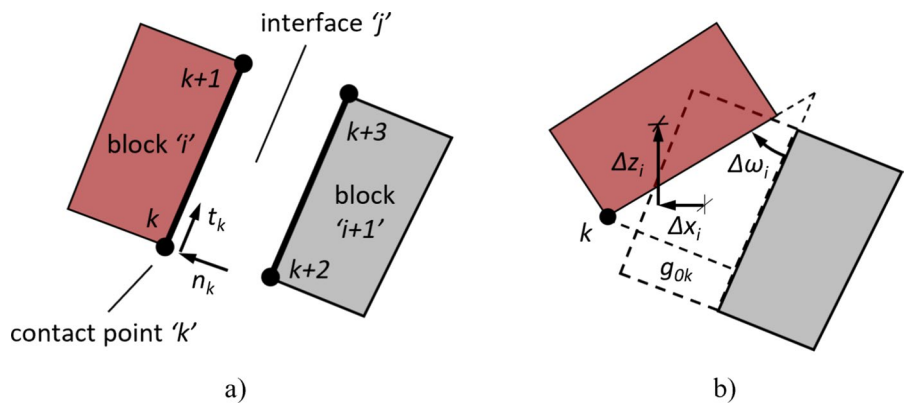

Fig. 4 **a** Internal forces and contact nodes at rigid blocks; **b** block displacements and contact gaps

the unit weight and volume of the blocks representing the arch voussoirs, respectively;
- $\boldsymbol{f_L}$ is the vector of live loads.

Figure 4 shows the internal forces n_k and t_k acting at the contact points, along with the block displacements Δx and the contact gaps $g_{0,k}$.

Problem (1) represents an extension of the classic lower bound formulation of limit analysis to a displaced configuration with contact gaps $\boldsymbol{g}_0$. The first constraint of the optimization problem ($\boldsymbol{A}_0\boldsymbol{c} = \boldsymbol{f_D} + \alpha\boldsymbol{f_L}$) corresponds to the matrix form of equilibrium conditions, whereas the second constraint ($\boldsymbol{Y}^{\mathbf{T}}\boldsymbol{c} \leq 0$) is the matrix expression of failure conditions.

Displacement increments associated to the failure mechanism obtained in (1) are derived from the Lagrange multipliers related to the solution of the following dual problem, corresponding to the upper bound formulation of limit analysis:

$$\begin{aligned} &\min\ -\boldsymbol{f}_D^{\mathbf{T}}\boldsymbol{\Delta x} \\ &\text{s.t.}\ \ \boldsymbol{f}_L^{\mathbf{T}}\boldsymbol{\Delta x} = \gamma \\ &\qquad \boldsymbol{A}_0^{\mathbf{T}}\boldsymbol{\Delta x} - \boldsymbol{Y}\lambda = \boldsymbol{g}_0,\ \lambda \geq 0 \end{aligned} \tag{2}$$

where λ is the (3c × 1) vector of non-negative flow multipliers of contact displacement increments.

For pushdown analyses with a rigid contact formulation, a formulation similar to that used in the pushover analyses was employed. In this case, as reported in [39, 50], the load multiplier was associated with the reaction at the movable block (R in Fig. 3a), which corresponds to the activation of the failure mechanism induced by the support displacement δ_z.

In the case of numerical simulations employing elastic contact interfaces, the following optimization problems were considered for pushover and pushdown analyses, respectively [15]:

$$\begin{aligned} &\max\ -\tfrac{1}{2}\boldsymbol{c}^{\mathbf{T}}\boldsymbol{C}\boldsymbol{c} - \boldsymbol{g}_0^{\mathbf{T}}\boldsymbol{c} \\ &\text{s.t.}\ \ \boldsymbol{A}_0\boldsymbol{c} = \boldsymbol{f} \\ &\qquad \boldsymbol{Y}^{\mathbf{T}}\boldsymbol{c} \leq 0 \end{aligned} \tag{3}$$

$$\begin{aligned} &\min\ \tfrac{1}{2}\boldsymbol{c}^{\mathbf{T}}\boldsymbol{C}\boldsymbol{c} - \boldsymbol{f}^{\mathbf{T}}\boldsymbol{\Delta x} \\ &\text{s.t.}\ \ \boldsymbol{A}_0^{\mathbf{T}}\boldsymbol{\Delta x} - \boldsymbol{Y}\lambda - \boldsymbol{C}\boldsymbol{c} = \boldsymbol{g}_0, \lambda \geq 0 \end{aligned} \tag{4}$$

where $\boldsymbol{C}$ is the matrix of contact compliances collecting submatrices $\boldsymbol{C_k} = diag\left(\ C_{n,k}\ \ C_{t,k}\ \right)$, with $C_{n,k} = 1/k_{n,k}$ and $C_{t,k} = 1/k_t$. The stiffnesses $k_{n,k}$ and $k_{t,k}$ are the normal and tangential stiffnesses at contact points k and are determined based on the interface stiffness $k_{n,j}$, expressed as N/mm^3. Considering that a four-node interface model is adopted, the normal contact stiffness $k_{n,k}$ is expressed as $k_{n,k} = \left(k_{n,j} \bullet l_j \bullet d_j\right)/4$, where l_j and d_j are the length and the depth of interface j, respectively. The tangential contact stiffness $k_{t,k}$ was assumed to be infinite, and a null value was assigned to $C_{t,k}$.

In problem (3), the vector of external loads $\boldsymbol{f}$ is expressed as the sum of dead and lateral loads, that is $\boldsymbol{f} = \boldsymbol{f_D} + \alpha\boldsymbol{f_L}$, where α is a known load multiplier associated with a load increment. In problem (4), the vector $\boldsymbol{f}$ includes only dead loads ($\boldsymbol{f} = \boldsymbol{f_D}$).

Problems (3) and (4) represent an extension of problems (1) and (2) to the case of an elastic contact formulation and, therefore, include terms associated to elastic energy in the objective function. Further details on the rigid block modelling approach and optimization-based formulations adopted in this work can be found in [15, 46].

3 Numerical simulations

3.1 Overview

The effect of support displacements on the response of the arch to lateral loads was evaluated by conducting different types of nonlinear static analyses. A preliminary pushdown analysis was performed to assess the ultimate displacement capacity of the arch under vertical support displacements. In this analysis, a vertical displacement δ_z was applied at the right support of the arch and increased monotonically until collapse occurred.

Subsequently, sequential pushdown-pushover analyses were conducted. In these analyses, lateral loads were applied on a series of deformed geometries of the arch resulting from the application of increasing values of δ_z, each representing a specific percentage of the collapse displacement due to vertical support movements. Four values of δ_z were considered: δ_{z1}, δ_{z2}, δ_{z3}, and δ_{z4}, corresponding to approximately 10%, 25%, 50% and 75% of the vertical collapse displacement. For comparison, an additional sequential analysis was performed considering the

arch in its undeformed configuration, i.e. without any vertical displacement imposed at the right support ($\delta_{z0}=0$ mm).

The preliminary pushdown analysis was performed using a rigid contact formulation, while the sequential analyses employed elastic and rigid contact formulations to assess the arch's behaviour before and after the activation of the collapse mechanism under lateral loads, respectively.

The response of the arch to lateral loads and support displacements was evaluated in terms of deformed geometries, collapse mechanisms, hinge positions, initial load multiplier α, and pushover curves. The pushover curves represent the arch's response to lateral loads and can be derived by plotting the load multiplier α against the horizontal displacement of a control point. In this work, where sequential analyses were performed, the pushover curves were obtained by plotting α against the horizontal relative displacement at the control point (CP in Fig. 3). This displacement, denoted as d_c, was computed with respect to the deformed configuration produced by the application of support displacements in the pushdown analysis. Significant values of d_c assessed in this study include the initial horizontal relative displacement ($d_{c,0}$) at the activation of the collapse mechanism ($\alpha=\alpha_0$), and the ultimate horizontal relative displacement (hereafter referred to as ultimate displacement capacity, $d_{c,u}$), which is obtained when the arch can no longer withstand lateral loads ($\alpha=0$).

The results of the nonlinear static analyses are presented in Sect. 3.2 for the preliminary pushdown analysis and in Sects. 3.3 and 3.4 for the sequential pushdown-pushover analyses. For the sequential analyses, the response of the arch to lateral loads was initially analysed for a representative value of δ_z, specifically δ_{z2} (see Sect. 3.3) The objectives of this analysis were to: (i) thoroughly investigate the evolution of the arch deformed geometry and hinge configuration from support displacements to the ultimate condition under lateral loads ($\alpha=0$), (ii) outline the methodology used to construct pushover curves by integrating results from elastic and rigid contact formulations, and (iii) validate numerical predictions through comparison with analytical results. Subsequently, a sensitivity analysis was performed to assess how varying the magnitude of the vertical support displacement δ_z affected the response of the arch to lateral loads (see Sect. 3.4).

3.2 Preliminary pushdown analysis

The preliminary pushdown analysis was performed by applying displacement increments of 1.0 mm to the movable block shown in Fig. 3a. Figure 5a shows the initial hinge configuration at the first displacement increment. Consistent with previous findings in the literature (see [28, 32, 39, 40, 51]), the arch responds to the imposed vertical displacement by opening three hinges, A, B and C, located in the sequence I-E-E from left to right, where E and I indicate extrados and intrados, respectively. Hinge A is located at the intrados at the left haunch (between 7 and 8th blocks), whereas the consecutive hinges B and C appear at the

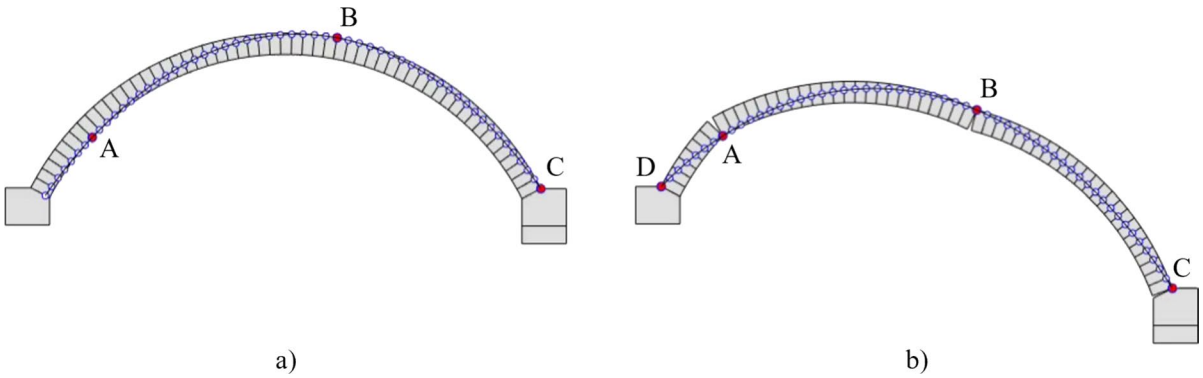

Fig. 5 Arch geometries and hinge configurations obtained from the pushdown analysis: **a** initial at first displacement increment; **b** final at collapse

extrados close to the crown (between 32nd and 33rd blocks) and at the right support, respectively.

Generally, hinges A, B, and C remain in their positions as support displacements increase, with the exception of hinge B, which shifts left by one voussoir at the onset of the analysis. Collapse occurs when a fourth hinge, D, appears at the extrados at the left support (Fig. 5b). The collapse displacement is 113 mm, which corresponds to 21.2% of the arch's span.

The results described above are in agreement with those reported in [39], where the same small-scale arch investigated in this work was analysed using different micro-modelling strategies.

Figure 6 shows the deformed geometries of the arch analysed in the sequential pushover-pushdown analyses (Sects. 3.3 and 3.4). These geometries result from the application of four increasing values of vertical displacement δ_z: $\delta_{z1}=11$ mm, $\delta_{z2}=28$ mm, $\delta_{z3}=57$ mm, and $\delta_{z4}=85$ mm, approximately corresponding to 10%, 25%, 50% and 75% of the vertical collapse displacement, respectively. Notably, although the positions of hinges A, B, and C do not change, the overall geometry of the arch undergoes significant changes as the vertical displacement δ_z increases. This underscores the importance of evaluating how variations in geometry affect the arch's response to lateral loads.

3.3 Sequential pushdown-pushover analyses for $\delta_{z2}=28$ mm

This section presents the results of the sequential pushdown-pushover analysis conducted for $\delta_{z2}=28$ mm. A first sequential analysis was conducted to evaluate the arch's response from the application of support displacements to the activation of the collapse mechanism under lateral loads ($\alpha=\alpha_0$). In this analysis, an elastic contact formulation was employed, assuming a high normal stiffness value ($k_n=1000$ N/mm^3) for the interfaces.

Figure 7 illustrates the evolution of the arch's geometry as it transitions from the application of support displacements (Fig. 7a) to the activation of the collapse mechanism under lateral loads (Fig. 7d). A gradual change in the hinge configuration is observed. After the application of vertical support displacements, the arch exhibits three hinges, A, B and C, positioned according to the sequence I-E-E (Fig. 7a). As the lateral loads are applied and the corresponding

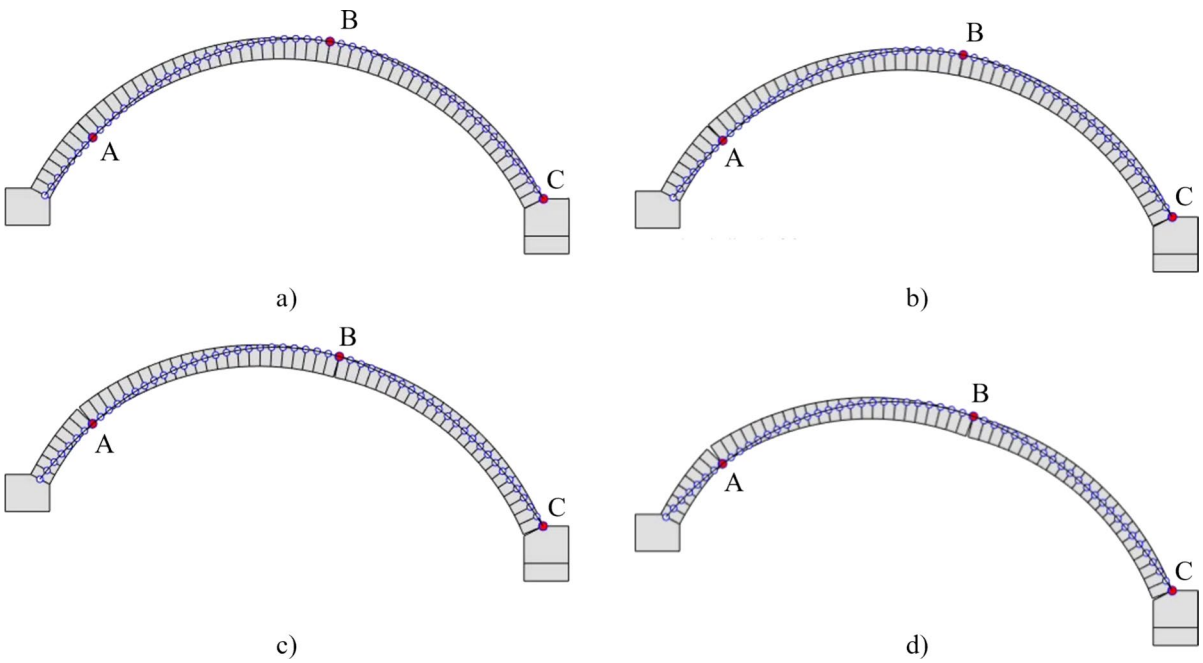

Fig. 6 Deformed geometries resulting from the application of increasing values of the vertical displacement δ_z: **a** $\delta_{z1}=11$ mm; **b** $\delta_{z2}=28$ mm; **c** $\delta_{z3}=57$ mm; **d** $\delta_{z4}=85$ mm

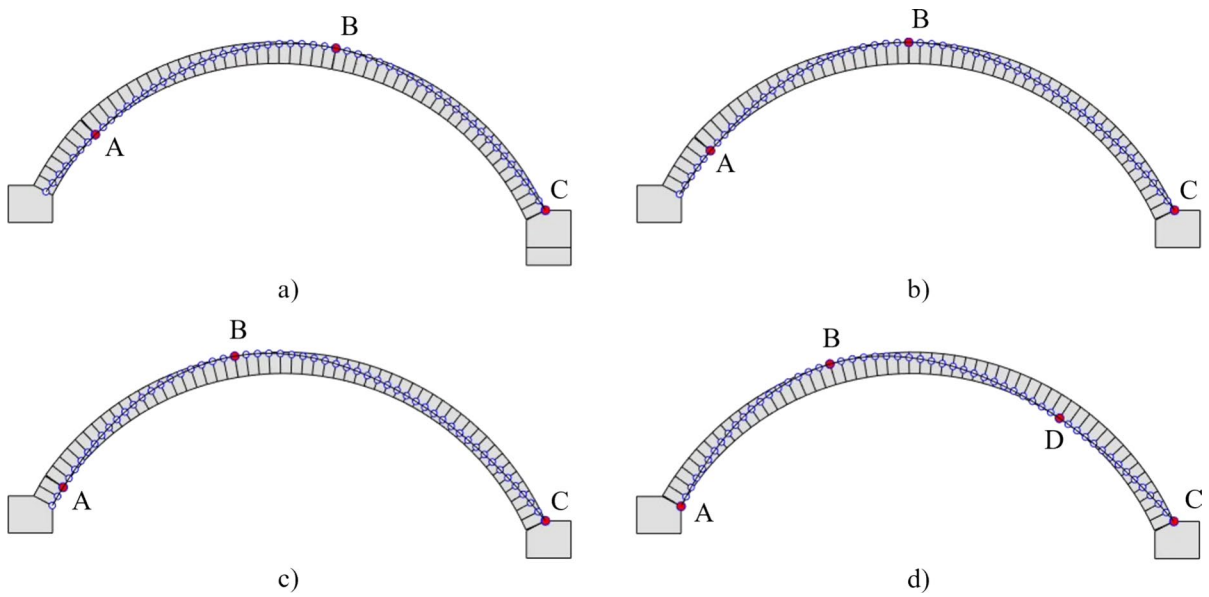

Fig. 7 Rigid block model with elastic contact formulation—evolution of the hinge configuration from the application of vertical support displacements to the activation of the collapse mechanism under lateral loads: **a** $\alpha=0$, $d_c=0.00$ mm; **b** $\alpha=0.14$, $d_c=0.52$ mm; **c** $\alpha=0.22$, $d_c=0.86$ mm; **d** $\alpha=\alpha_0=0.31$, $d_c=d_{c,0}=1.03$ mm

load multiplier α increases (Fig. 7c,d), hinges A and B move towards the left support, causing the thrust line to approach the intrados at the right haunch. When the thrust line touches the arch intrados at the right haunch (Fig. 7d), an additional hinge, D, appears. This results into a four-hinge configuration with hinges located alternately between the intrados and extrados according to the sequence I-E-I-E.

A second sequential analysis was performed to investigate the arch's response from the activation of the collapse mechanism to the ultimate condition, where the arch can no longer withstand any lateral load ($\alpha=0$). In this analysis, a rigid contact formulation was employed for the interfaces.

Figure 8 shows the evolution of the arch's deformed geometry during this transition from the activation of the collapse mechanism (Fig. 8a) to the ultimate condition (Fig. 8d). At the activation of the collapse mechanism ($\alpha=\alpha_0$ and $d_c=d_{c,0}$), hinges A, B and C are open, while hinge D is closed (Fig. 8a). When the horizontal relative displacement d_c exceeds $d_{c,0}$, hinge D starts to opens, initiating motion, and the mechanism evolves (Fig. 8b,c) until it reaches an ultimate configuration in which the arch can no longer withstand any lateral load ($\alpha=0$, Fig. 8d). This configuration is still characterized by four hinges located according to the sequence I-E-I-E.

Figure 9 and Table 1 compare the results obtained from the sequential analyses using both the elastic contact formulation (ECF) and the rigid contact formulation (RCF). Specifically, Fig. 9 presents the pushover curves, while Table 1 reports the values of the initial load multiplier α_0 and initial horizontal relative displacement $d_{c,0}$.

As shown in Fig. 9, the curve derived using elastic contact interfaces with high normal stiffness is characterized by a single branch with a monotonically ascending trend. The horizontal relative displacement d_c at the control point increases with the load multiplier α until the collapse mechanism is triggered at $\alpha=\alpha_0$. The dashed branch of the curve represents non-convergent numerical solutions and is included only to demonstrate that the load multiplier α does not increase beyond α_0.

The curve obtained using the rigid contact formulation has two branches. The dashed branch represents the evolution of the arch configuration from the application of support displacements to the activation of the collapse mechanism under lateral loads ($\alpha=\alpha_0$). The solid branch corresponds to the progression of the mechanism from activation to the

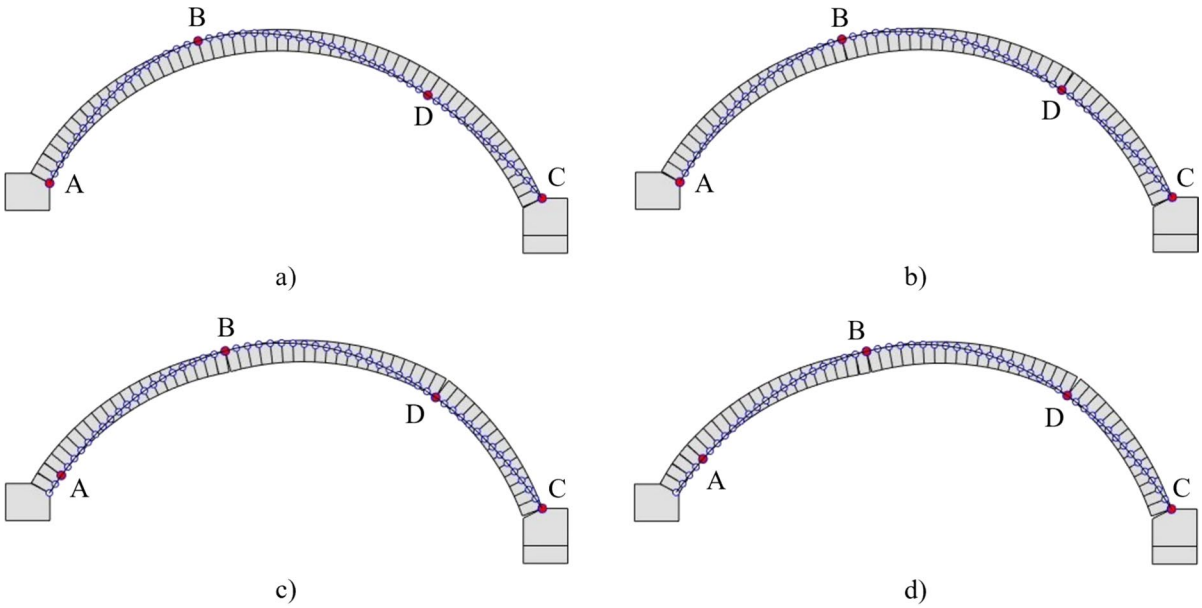

Fig. 8 Rigid block model with rigid contact formulation—evolution of the hinge configuration from the activation of the collapse mechanism to the ultimate condition: **a** $\alpha=\alpha_0=0.31$; $d_c=d_{c,0}=1.00$ mm; **b** $\alpha=0.19$; $d_c=5.00$ mm; **c** $\alpha=0.07$; $d_c=9.00$ mm; **d** $\alpha=0$, $d_c=d_{c,u}=11.1$ mm

ultimate configuration corresponding to $\alpha=0$. This branch displays a monotonically descending trend: the load multiplier α decreases with increasing d_c until it reaches zero and the arch can no longer withstand any lateral load.

As depicted in Fig. 9, the curves from the two contact formulations intersect at a point corresponding to the activation of the collapse mechanism. The values of α_0 for both formulations are identical, while the values of $d_{c,0}$ differ by only 3% (see Table 1). Additionally, the same hinge position is observed regardless of the contact formulation employed (compare Figs. 7d and 8a).

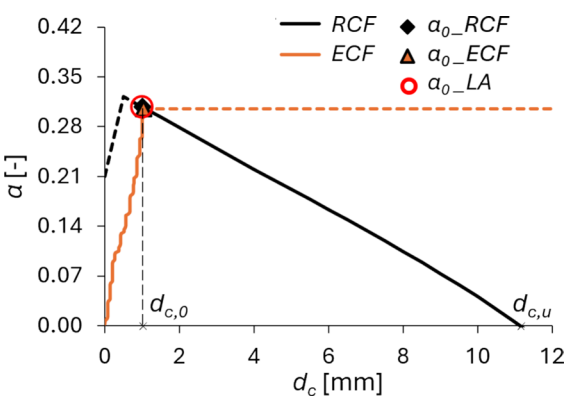

Fig. 9 Pushover curves and initial load multiplier α_0 obtained using both elastic (ECF) and rigid (RCF) contact formulations. Comparison with the results from graphic kinematic limit analysis (LA) is provided for α_0

These results indicate that the elastic interfaces with high normal stiffness behave as rigid interfaces. Consequently, the pushover curve of the arch under lateral loads can be considered as consisting of two branches: one ascending and one descending, derived using elastic and rigid contact formulations, respectively. The dashed branch obtained using the rigid contact formulation, corresponding to values of α smaller than α_0, should be disregarded, as it represents kinematically non-admissible deformed configurations of the arch.

Looking at Fig. 9, it is interesting to note that a non-zero value of the initial horizontal relative displacements $d_{c,0}$ is associated with the change in the arch geometry and hinge configuration from the application of support displacements ($d_c=0$, see Fig. 6b and Fig. 7a) to the activation of the collapse mechanism under lateral loads ($\alpha=\alpha_0$ and $d_c=d_{c,0}$, see Fig. 7d and Fig. 8a).

Table 1 Initial load multiplier α_0 and the corresponding initial horizontal relative displacement $d_{c,0}$ obtained analytically from graphic kinematic limit analysis (LA) and numerically using rigid (RCF) and elastic (ECF) contacts formulations

	α_0		$d_{c,0}$	
	Result [-]	Difference from LA [%]	Result [-]	Difference from LA [%]
Limit analysis (LA)	0.31	–	1.00	–
Rigid contact formulation (RCF)	0.31	−0.04	1.00	0.25
Elastic contact formulation (ECF)	0.31	−0.94	1.03	3.54

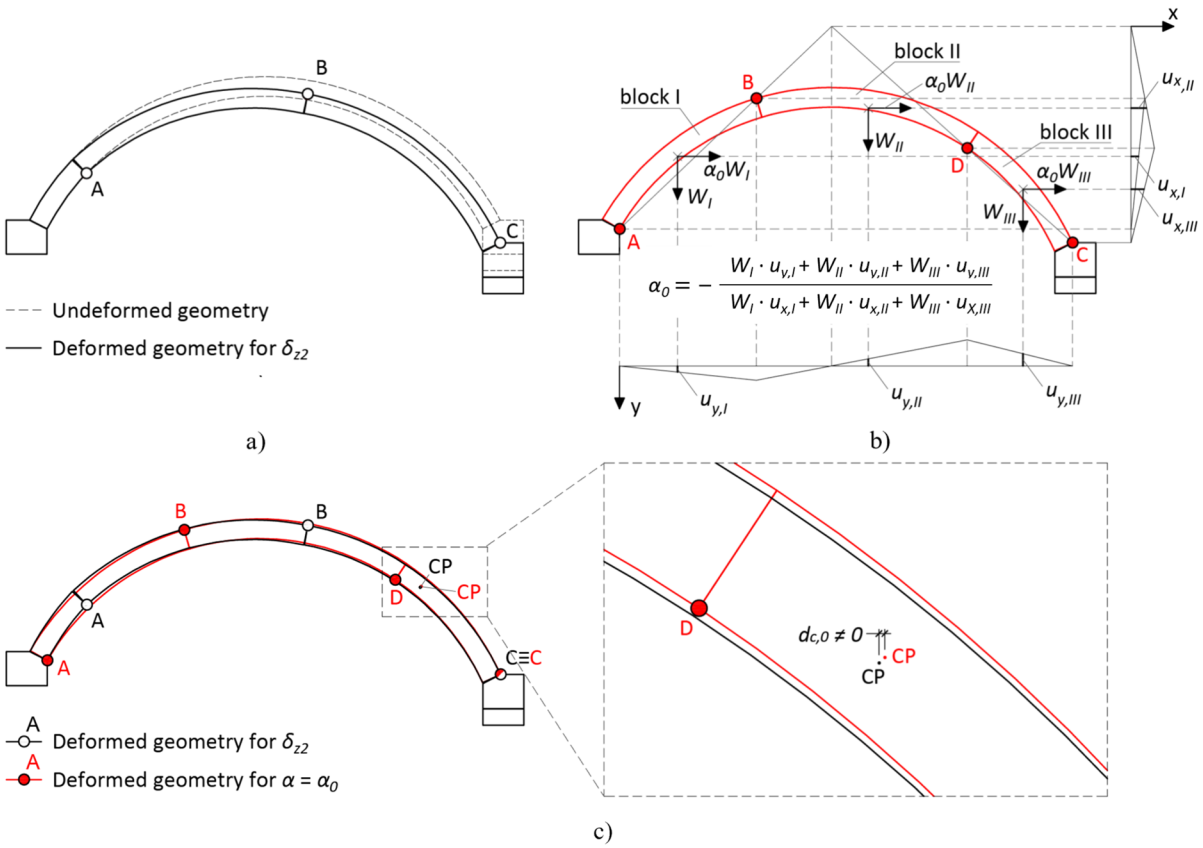

Fig. 10 **a** Deformed geometry resulting from the application of the vertical support displacement $\delta_{z2} = 28$ mm; **b** application of the Principle of Virtual Works to the deformed geometry obtained at the activation of the collapse mechanism under lateral loads (W_i are the self-weights of the blocks $i = I, II, III$; $u_{y,i}$ and $u_{x,i}$ are the vertical and horizontal virtual displacements of the centres of gravity of the blocks, respectively); **c** comparison between the deformed geometries shown in **a** and **b** and horizontal displacement of the control point CP.

To gain deeper insight into this outcome and to validate the numerical results, the change in the hinge configuration was further investigated through graphic kinematic limit analysis (see [52]). For this purpose, two deformed geometries of the arch were analysed within a CAD environment (see Fig. 10a and b).

The first geometry (Fig. 10a) results from the application of a vertical displacement of 28 mm at the right support of the arch. This geometry was

created by dividing the arch into three blocks based on the positions of hinges A, B and C, and by rotating blocks A-B and B-C around hinges A and C, respectively. The analytical hinge positions were assumed to correspond to the numerical positions shown in Fig. 6b.

The second geometry (Fig. 10b) was used for the calculation of the initial load multiplier α_0. It corresponds to a four-hinge configuration, with hinges A, B, C and D positioned as obtained in the numerical model at the activation of the collapse mechanism under lateral loads (Fig. 8a). This deformed geometry results from a shift in the positions of hinges A and B compared to their locations at the application of support displacements (Fig. 10a). It was obtained by rotating block I (see Fig. 10b) around hinge A and treating blocks II and III as a single block rotating around hinge C. No relative rotation was assumed between blocks II and III, as hinge D was considered closed and was used only for calculating the initial load multiplier α_0. To calculate α_0, the Principle of Virtual Works was applied the deformed geometry of the arch (see Fig. 10b).

Figure 10c compares the two deformed geometries of the arch depicted in Fig. 10a and b. By examining the positions of the control point CP in the two CAD configurations, it is evident that the control point undergoes a non-zero horizontal displacement $d_{c,0}$ when the arch transitions from the configuration due to support displacements (coloured in black) to the configuration under lateral loads (coloured in red).

The analytical value of $d_{c,0}$ shows good agreement with the numerical results, with differences of less than 4% for both contact formulations adopted (see Table 1). Similarly, the analytical value of the initial load multiplier α_0 deviates by less than 1% from the numerical predictions. These results validate the numerical outcomes and confirm that the change in the arch's deformed geometry resulting from the sequential application of support displacements and lateral loads is accompanied by a non-zero initial horizontal relative displacement $d_{c,0}$.

3.4 Sensitivity analysis to the magnitude of vertical support displacements

This section presents the results obtained from the sequential pushdown-pushover analyses as the vertical displacement δ_z increases from $\delta_z = 0$ mm to $\delta_{z4} = 85$ mm (see Sect. 3.1). All results, including deformed geometries of the arch, hinge positions, and values of α_0, d_{c0}, $d_{c,u}$, as well as the descending branch of the pushover curves, were obtained adopting a rigid contact formulation for the interfaces. Only the ascending branch of the pushover curve was derived using elastic contact interfaces with very high stiffness (see Sect. 3.1).

For each value of δ_z, Fig. 11 shows the deformed geometries of the arch at the activation of the collapse mechanism ($\alpha = \alpha_0$, on the left) and when the arch can no longer withstand any horizontal action ($\alpha = 0$, on the right). Table 2 reports the positions of hinges A, B, C and D in both configurations. The joints where the hinges appear are numbered sequentially from left to right, with joint No. 1 located at the left support.

As depicted in Fig. 11 on the left, the application of support displacements does not alter the failure mode of the arch under lateral loads. Regardless of δ_z, the arch consistently exhibits a four-hinge configuration with hinges positioned in the sequence I-E-I-E at the activation of the collapse mechanism. However, the hinge position depends on the magnitude of the vertical displacement δ_z. For $\delta_{z1} = 11$ mm and $\delta_{z2} = 28$ mm, the position of hinges A, B, C and D is the same as that obtained for $\delta_{z0} = 0$ mm (see Fig. 11a–c on the left). Conversely, for $\delta_{z3} = 57$ mm and $\delta_{z4} = 85$ mm, hinges A and B are located closer to mid-span than they are for $\delta_{z0} = 0$ mm (see Fig. 11d, e on the left).

For every value of δ_z, hinge D remains closed at the activation of the collapse mechanism and opens, initiating motion, when the horizontal relative displacement d_c exceeds $d_{c,0}$. As d_c continues to increase, the collapse mechanism progresses until it reaches an ultimate configuration in which the arch can no longer withstand lateral loads ($\alpha = 0$, Fig. 11 on the right). In this configuration, hinges A, B, C and D are still arranged in the sequence I-E-I-E. However, their specific positions may differ from those observed at the activation of the collapse mechanism, as the hinges can shift with increasing d_c.

As shown in Table 2, the movement of the hinges is influenced by the magnitude of the imposed displacement δ_z. For $\delta_{z,0} = 0$ mm, $\delta_{z1} = 11$ mm and $\delta_{z2} = 28$ mm, hinges A and B change position with increasing d_c, while hinges C and D do not move. For $\delta_{z3} = 57$ mm and $\delta_{z4} = 85$ mm, none of the four hinges A, B, C and D move.

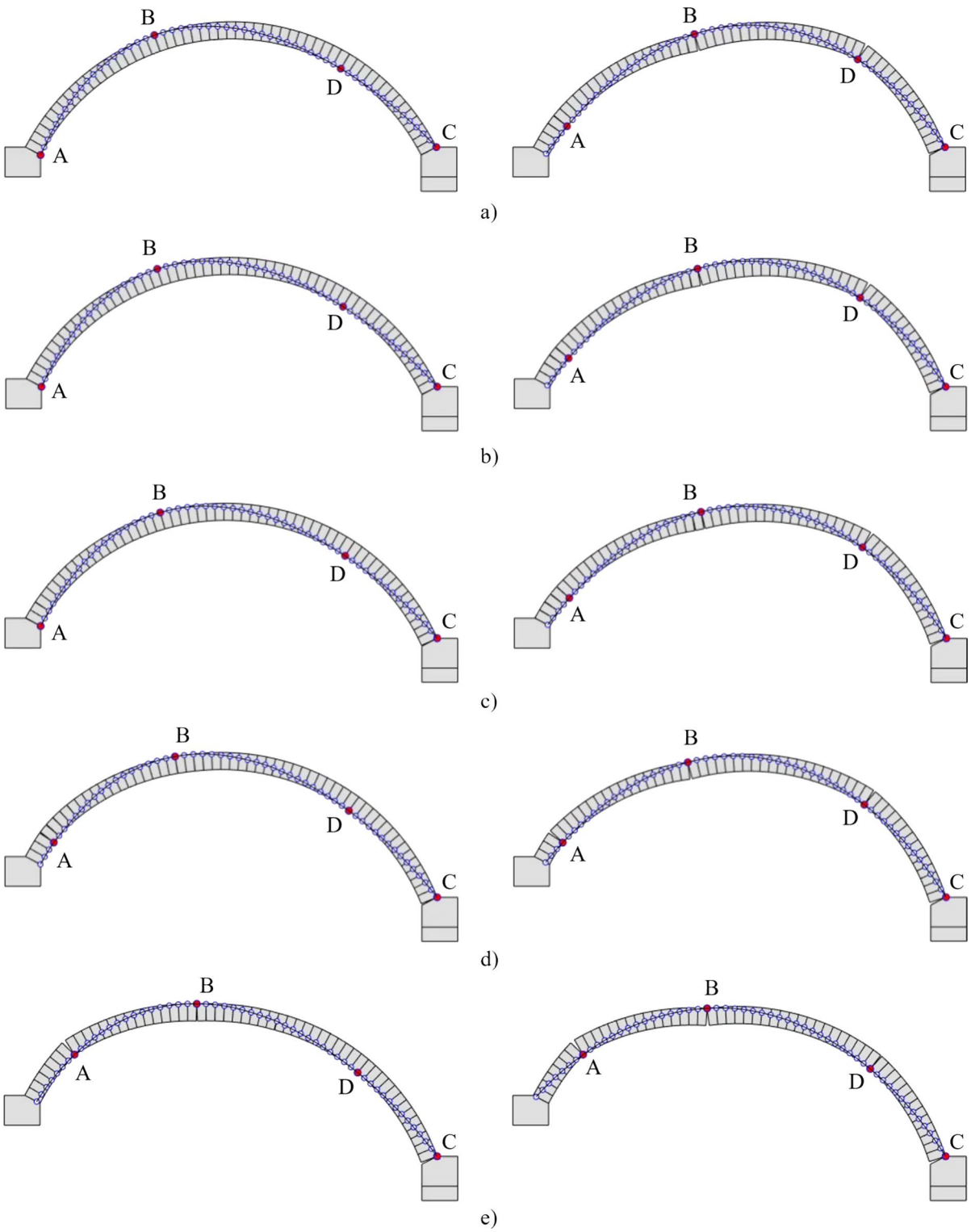

Fig. 11 Deformed configurations at the activation of the collapse mechanism (for $\alpha = \alpha_0$, on the left), and when the arch is no longer able to withstand lateral loads ($\alpha = 0$, on the right): **a** $\delta_{z0} = 0$ mm; **b** $\delta_{z1} = 11$ mm; **c** $\delta_{z2} = 28$ mm; **d** $\delta_{z3} = 57$ mm; **e** $\delta_{z4} = 85$ mm

Table 2 Hinge position at the activation of the collapse mechanism ($\alpha=\alpha_0$) and for $\alpha=0$ when varying the magnitude of the vertical displacement δ_z (the joints where the hinges appear are numbered from left to right, with joint No. 1 located at the left support)

	Joint No.									
	δ_{z0}		δ_{z1}		δ_{z2}		δ_{z3}		δ_{z4}	
	$\alpha=\alpha_0$	$\alpha=0$	$\alpha=\alpha_0$	$\alpha=0$	$\alpha=\alpha_0$	$\alpha=0$	$\alpha=\alpha_0$	$\alpha=0$	$\alpha=\alpha_0$	$\alpha=0$
Hinge A	1	5	1	5	1	5	4	4	8	8
Hinge B	20	23	20	23	20	23	21	21	23	23
Hinge C	56	56	56	56	56	56	56	56	56	56
Hinge D	42	42	42	42	42	42	42	42	43	43

Further insights into hinge position in the ultimate configuration ($\alpha=0$) can be derived from Table 2. For $\delta_{z1}=11$ mm and $\delta_{z2}=28$ mm, the positions of all four hinges A, B, C and D match those obtained when no vertical support displacements are imposed ($\delta_{z0}=0$ mm). In contrast, for $\delta_{z3}=57$ mm and $\delta_{z4}=85$ mm, the hinge positions correspond to those observed for $\delta_{z0}=0$ mm only for hinges C and D in the case of δ_{z3}, and for hinges B and C in the case of δ_{z4}.

Figure 12 presents the pushover curves obtained for δ_{z0}, δ_{z1}, δ_{z2}, δ_{z3}, and δ_{z4}. Despite the different values of vertical displacement imposed prior to applying lateral loads, all curves exhibit a similar overall trend. As d_c increases, the load multiplier α monotonically increases until it reaches its maximum value α_0, then steadily decreases until it reaches zero. The curves obtained for δ_{z1}, δ_{z2}, δ_{z3}, and δ_{z4} follow a similar pattern as the curve obtained for δ_{z0}. However, for δ_{z0}, α increases with a constant null horizontal displacement d_c. This result was expected, as $d_{c,0}$ is necessarily zero when no support displacements are imposed and lateral loads are applied to the undeformed geometry of the arch.

Figure 13 plots the initial load multiplier α_0 and the initial horizontal relative displacement $d_{c,0}$ as functions of the imposed vertical displacement δ_z. As shown in Fig. 13a, the application of vertical support displacements leads to a decrease in the initial load multiplier α_0 and, therefore, a reduction in the horizontal action triggering the collapse mechanism compared to the scenario without support displacements. The initial load multiplier α_0 decreases progressively as δ_z increases. Specifically, the reduction in α_0 compared to $\alpha_{0,0}$ (0.36) is 7%, 16%, 30% and 40% for δ_{z1}, δ_{z2}, δ_{z3}, and δ_{z4}, respectively.

As depicted in Fig. 13b, the initial horizontal relative displacement $d_{c,0}$ increases as δ_z increases up to

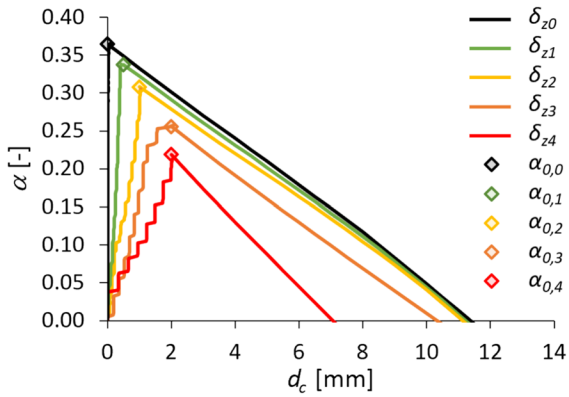

Fig. 12 Pushover curves obtained from sequential push-down-pushover analyses for increasing values of the vertical displacement δ_z ($\delta_{z0}=0$ mm; $\delta_{z1}=11$ mm; $\delta_{z2}=28$ mm; $\delta_{z3}=57$ mm; $\delta_{z4}=85$ mm)

δ_{z3}, and then remains constant. This result indicates that the horizontal relative displacement associated with transition from the three-hinge configuration caused by vertical support displacements to the four-hinge configuration under lateral loads generally increases with the imposed vertical displacement δ_z.

Lastly, Fig. 14 shows the variation in the ultimate displacement capacity under lateral loads, $d_{c,u}$, as a function of the imposed vertical displacement δ_z. The application of support displacements reduces the ultimate displacement capacity of the arch, which progressively decreases as δ_z increases. For δ_{z1} and δ_{z2}, the reduction in $d_{c,u}$ compared to the value obtained when no support displacements are imposed is minimal (1.3% and 2.2%, respectively), indicating that $d_{c,u}$ is only slightly affected by the application of vertical support displacements. In contrast, for δ_{z3} and δ_{z4}, the decrease is significant, amounting to 9.2% and 37.9%, respectively.

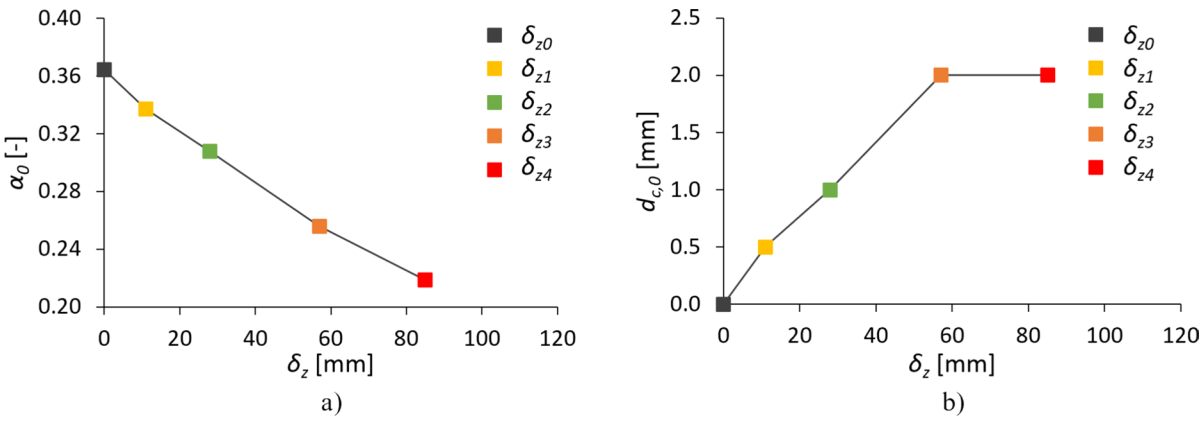

Fig. 13 **a** Initial load multiplier at the activation of the collapse mechanisms under later loads, α_0, vs. vertical displacement at the right support, δ_z; **b** Initial horizontal relative displacement $d_{c,0}$ vs. vertical displacement at the right support, δ_z

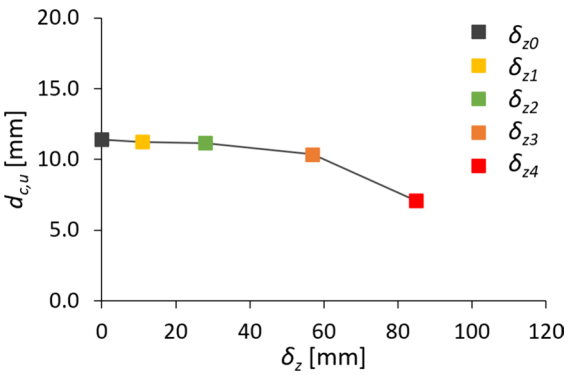

Fig. 14 Ultimate displacement capacity under lateral loads, $d_{c,u}$ vs. vertical displacement at the right support, δ_z

4 Conclusions

In this paper, the effect of large support displacements on the response of masonry arches to lateral loads was investigated by analysing a small-scale segmental dry-joint masonry arch subjected to vertical support displacements. The arch was modelled as an assemblage of rigid voussoirs connected by no-tension friction interfaces, using a rigid block modelling approach developed by one of the authors. Both rigid and elastic contact formulations were adopted for the interfaces. The response of the arch to vertical support displacements and lateral loads, applied in one direction, was assessed by performing different types of nonlinear static analyses. These included a preliminary pushdown analysis under support displacements, and sequential pushdown-pushover analyses, where lateral loads were applied on a series of deformed geometries of the arch resulting from the application of increasing values of vertical support displacements.

The results of the numerical simulations provided new conclusions on the response of the arch to lateral loads. Firstly, the arch geometry and hinge configuration were observed to gradually evolve from the application of support displacements to the activation of the collapse mechanism under lateral loads. Notably, the transition from a three-hinge configuration (I-E-E) due to vertical support displacements to a four-hinge configuration caused by lateral loads (I-E-I-E) was associated with a non-zero value of the initial horizontal relative displacement at the control point, $d_{c,0.}$ This parameter, equal to zero when lateral loads are applied to the undeformed geometry of the arch, increased as the vertical displacement δ_z imposed at the right support increased.

Secondly, the pushover curves generated by applying lateral loads to a deformed arch geometry were shown to consist of two branches: one ascending and one descending. These branches were derived using elastic and rigid contact formulations, respectively. The ascending branch represented the evolution of the arch configuration from the application of support displacements to the activation of the collapse mechanism under lateral loads ($\alpha = \alpha_0$). The descending branch corresponded to the progression of the mechanism from activation to the ultimate configuration corresponding to $\alpha = 0$.

Thirdly, the application of support displacements did not affect the activation of the collapse mechanism under lateral loads. Despite some differences in the hinge positions and movements obtained as δ_z varied, the arch consistently exhibited the same collapse mechanism obtained for δ_{zo}, namely a four-hinge mechanism with hinges alternating between the intrados and extrados. Furthermore, regardless of the value of δ_z imposed at the right support, the pushover curve showed the same overall trend obtained when no support displacements were applied, always including an ascending branch followed by a descending branch.

Lastly, the sensitivity analysis conducted while varying δ_z showed that the magnitude of vertical support displacements significantly influences both the initial load multiplier α_0 and the ultimate displacement capacity $\delta_{c,u}$ of the arch under lateral loads. As δ_z increased, both α_0 and $\delta_{c,u}$ were observed to decrease. The reduction in the ultimate displacement capacity $\delta_{c,u}$ compared to the value obtained for δ_{z0} was significant only for support displacements equal to 50% of 75% of the vertical collapse displacement. In contrast, the decrease in the initial load multiplier α_0 was notable for every δ_z, ranging from 7% to 40% for δ_{z1} and δ_{z4}, respectively. This result underscores the importance of considering the actual deformed geometry of arches when analysing their response to lateral loads. Ignoring the deformations caused by support displacements can lead to a substantial overestimation of the lateral load triggering the collapse mechanism, and, consequently, an overestimation of the arch capacity to withstand seismic actions.

Future work will focus on investigating the effect of vertical, horizontal and inclined support displacements on the response of masonry arches to lateral loads. To extend the findings of this work to a wider range of arches structures, arches with varying geometries, shapes and materials will be analysed. Additionally, the influence of support displacements on the response of masonry arches with elastic interfaces will be evaluated. Recent studies by the authors (see [15, 41]) have demonstrated that the joint deformability can significantly affect the response of masonry structures to large support displacements and lateral loads. Finally, the arch's behaviour under the sequential application of support displacements and lateral loads will be investigated by applying lateral loads in two opposite directions to simulate the cyclic nature of seismic actions.

Author contribution Chiara Ferrero: Conceptualization, methodology, formal analysis, investigation, writing—original draft, writing—review & editing, visualization. Francesco Portioli: conceptualization, methodology, formal analysis, software, validation, writing—review & editing. Chiara Calderini: conceptualization, writing—review & editing, supervision.

Funding Open access funding provided by Università degli Studi di Napoli Federico II within the CRUI-CARE Agreement.

Data availability Data will be made available on request.

Declaration

Competing interests The authors declare no competing interests.

References

1. Brandonisio G, Lucibello G, Mele E, De Luca A (2013) Damage and performance evaluation of masonry churches in the 2009 L'Aquila earthquake. Eng Fail Anal 34:693–714
2. Cattari S, Degli Abbati S, Ferretti D, Lagomarsino S, Ottonelli D, Tralli A (2014) Damage assessment of fortresses after the 2012 Emilia earthquake (Italy). Bull Earthq Eng 12:2333–2365
3. Cattari S, Degli Abbati S, Ferretti D, Lagomarsino S, Ottonelli D (2012) Rossi M (2012) The seismic behaviour of ancient masonry buildings after the earthquake in Emilia (Italy) on May 20th and 29th. Ingegneria Sismica 29(2):87–111
4. Penna A, Calderini C, Sorrentino L, Carocci CF, Cescatti E, Sisti R, Borri A, Modena C, Prota A (2019) Damage to churches in the 2016 central Italy earthquakes. Bull Earthq Eng 17(10):5763–5790

5. da Porto F, Silva B, Costa C, Modena C (2012) Macro-scale analysis of damage to churches after earthquake in Abruzzo (Italy) on April 6, 2009. J Earthquake Eng 16(6):739–758
6. Guerreiro L, Azevedo J, Proenca J, Bento R, Lopes M (2000) Damage in ancient churches during the 9th of July 1998 Azores earthquake. In: Proceedings of the 12th world conference on earthquake engineering, Auckland, New Zealand, paper no. 780.
7. Romão X, Costa AA, Paupério E, Rodrigues H, Vicente R, Varum H, Costa A (2013) Field observations and interpretation of the structural performance of constructions after the 11 May 2011 Lorca earthquake. Eng Fail Anal 34:670–692
8. Lagomarsino S, Podestà S (2004) Seismic vulnerability of ancient churches. Part 1: damage assessment and emergency planning. Earthq Spectra 20(2):377–394
9. Lagomarsino S, Podestà S (2004) Seismic vulnerability of ancient churches Part 2: statistical analysis of surveyed data and methods for risk analysis. Earthq Spectra 20(2):395–412
10. Alexakis H, Makri N (2014) Limit equilibrium analysis and the minimum thickness of circular masonry arches to withstand lateral inertial loading. Arch Appl Mech 84:757–772
11. Cavalagli N, Gusella V, Severini L (2016) Lateral loads carrying capacity and minimum thickness of circular and pointed masonry arches. Int J Mech Sci 115–116:645–656
12. DeJong MJ, De Lorenzis L, Adams S, Ochsendorf JA (2008) Rocking stability of masonry arches in seismic regions. Earthq Spectra 24(4):847–865
13. Dimitri R, Tornabene F (2015) A parametric investigation of the seismic capacity for masonry arches and portals of different shapes. Eng Fail Anal 52:1–34
14. Misseri G, DeJong M, Rovero L (2018) Experimental and numerical investigation of the collapse of pointed masonry arches under quasi-static horizontal loading. Eng Struct 173:180–190
15. Portioli FPA, Cascini L, Landolfo R, Lourenço PB (2023) An optimization-based rigid block modeling approach to seismic assessment of dry-joint masonry structures subjected to settlements. Soil Dyn Earthq Eng 166:107760
16. Calderini C, Lagomarsino S (2014) Seismic response of masonry arches reinforced by tie-rods: static tests on a scale model. J Struct Eng 141(5).
17. Como M, Coccia S, Di Carlo F (2019) Dyanmic response of rocking masonry circular arches. In: COMPDYN 2019 proceedings (pp.622–632). National Technical University of Athens
18. Stockdale G, Tiberti S, Camilletti D, Sferrazza PG, Habieb AB, Bertolesi E, Milani G, Casolo S (2018) Kinematic collapse load calculator: Circular arches. SoftwareX 7:174–179
19. Cavalagli N, Gusella V, Liberotti R (2020) Effect of shape uncertainties on the collapse condition of the circular masonry arch. In: Abali B, Giorgio I (eds) Developments and novel approaches in nonlinear solid body mechanics. Advanced structured materials, vol 130. Springer, Cham. https://doi.org/10.1007/978-3-030-50460-1_27
20. Cavalagli N, Gusella V, Liberotti R (2020) The role of shape irregularities on the lateral loads bearing capacity of circular masonry arches. In: Carcaterra A, Paolone A, Graziani G (eds) Proceedings of XXIV AIMETA conference 2019. AIMETA 2019. Lecture notes in mechanical engineering. Springer, Cham. https://doi.org/10.1007/978-3-030-41057-5_164.
21. Zizi M, Cacace D, Corlito V, Rouhi J, de Matteis G (2021) A preliminary structural analysis of typical arches of Italian gothic churches. In Gambardella C, Cennamo C, Germanà ML, Shahidan MF, Bougdah H (eds) Advances in utopian studies and sacred architecture; Springer: Cham, Switzerland; pp. 65–77
22. Ferrero C, Degli Abbati S, Cattari S, Lagomarsino S (2024) A novel strategy for the equivalent frame modelling of masonry arches in historic buildings: application to a case study. Int J Arch Heritage. https://doi.org/10.1080/15583058.2024.2385970
23. Ferrero C, Cambiaggi L, Vecchiattini R, Calderini C (2021) Damage assessment of historic masonry churches exposed to slow-moving. Int J Arch Heritage 15(8):1170–1195
24. Ferrero C, Sacco GLS, Ferrero M, Battini C, Calderini C (2023) Coupled deformation and structural analysis for the damage assessment of cultural heritage buildings: the case of a masonry church exposed to slow-moving landslides. In: Proceedings of the 13th international conference on structural analysis of historical constructions, Kyoto, Japan.
25. Roca P, Lourenço PB, Gaetani A (2020) Historic construction and conservation – materials, systems and damage. Taylor and Francis
26. Ochsendorf JA (2006) The masonry arch on spreading supports. Struct Eng 84(2).
27. Ferrero C, Cambiaggi L, Calderini,C, Vecchiattini R (2022) Historic masonry churches exposed to slow-moving landslides: a critical damage assessment. In: Proceedings of the third international symposium on geotechnical engineering for the preservation of monuments and historic sites, Naples, Italy.
28. Romano A, Ochsendorf JA (2009) The mechanics of gothic masonry arches. Int J Archit Heritage 4(1):59–82. https://doi.org/10.1080/15583050902914660
29. Coccia S, Di Carlo F, Rinaldi Z (2015) Collapse displacements for a mechanism of spreading-induced supports in a masonry arch. Int J Adv Struct Eng 7:307–320. https://doi.org/10.1007/s40091-015-0101-x
30. Di Carlo F, Coccia S (2020) Collapse state of elliptical masonry arches after finite displacements of the supports. Eng Failure Anal 114.
31. McInerney J, DeJong MJ (2015) Discrete element modeling of groin vault displacement capacity. Int J Archit Heritage 9(8):1037–1049. https://doi.org/10.1080/15583058.2014.923953
32. Galassi S, Misseri G, Rovero L, Tempesta G (2018) Failure modes prediction of masonry voussoir arches on moving supports. Eng Struct 173:706–717
33. Galassi S, Misseri G, Rovero L, Tempesta G (2019) Analysis of masonry pointed arches on moving supports: a numeric predictive model and experimental evaluations. In: Proceedings of the XXIV AIMETA conference 2019, 15–19 September 2019, Rome, Italy, 1–21

34. Galassi S, Misseri G, Rovero L (2021) Capacity assessment of masonry arches on moving supports in large displacements: numerical model and experimental validation. Eng Fail Anal
35. Iannuzzo A, Dell'Endice A, Van Mele T, Block P (2021) Numerical limit analysis-based modelling of masonry structures subjected to large displacements. Comput Struct 242
36. Zampieri P, Simoncello N, Pellegrino C (2017) Structural behaviour of masonry arch with no-horizontal springing settlement. Frattura Ed Integrità Strutturale 12(43):182–190. https://doi.org/10.3221/IGF-ESIS.43.14
37. Zampieri P, Cavalagli N, Gusella V, Pellegrino C (2018) Collapse displacements of masonry arch with geometrical uncertainties on spreading supports. Comput Struct 208:118–129
38. Alforno M, Monaco A, Venuti F, Calderini C (2021) Validation of simplified micro-models for the static analysis of masonry arches and vaults. Int J Archit Heritage 15(8):1196–1212
39. Ferrero C, Calderini C, Portioli F, Roca P (2021) Large displacement analysis of dry-joint masonry arches subject to inclined support movements. Eng Struct 238:112244
40. Ferrero C, Calderini C, Roca P (2022) Experimental analysis of dry-joint arches subject to inclined support displacements. Eng Struct 253:113804
41. Ferrero C, Calderini C, Roca P (2023) Effect of joint deformability on the experimental and numerical response of dry-joint masonry arches subjected to large support displacements. Eng Struct, 275(Part A), 115236
42. Galassi S, Misseri G, Rovero L (2022) Rigid-block analysis in large displacements of masonry arches on vertically moving supports. In: Pellegrino C, Faleschini F, Zanini MA, Matos JC, Casas JR, Strauss A (eds) Proceedings of the 1st conference of the european association on quality control of bridges and structures. EUROSTRUCT 2021. Lecture Notes in Civil Engineering, vol 200. Springer, Cham. https://doi.org/10.1007/978-3-030-91877-4_123.
43. Galassi S, Zampieri P (2023) A new automatic procedure for nonlinear analysis of masonry arches subjected to large support movements. Eng Struct, 276
44. Di Carlo F, Coccia S, Rinaldi Z (2018) Collapse load of a masonry arch after actual displacements of the supports. Arch Appl Mech 88:1545–1558
45. Simoncello N, Zampieri P, Zizi M, Rossi L, Pellegrino C (2022) Lateral response of damaged stand-alone arches: Tilting tests and rigid-block analysis. Eng Struct. https://doi.org/10.1016/j.engstruct.2022.114700
46. Portioli FPA (2023) DynABlock_2D: An optimization-based MATLAB application for rocking dynamics, nonlinear static and limit analysis of masonry block structures. SoftwareX 23:101454
47. Ferrero C, Portioli FPA, Calderini C (2024) Nonlinear static analysis of a scaled masonry arch subject to vertical settlements and lateral loads. In: Proceedings of the 18th world conference on earthquake engineering (WCEE2024), Milan, Italy.
48. Ferrero C (2021) Structural behaviour of masonry arches on moving supports: from on-site observation to experimental and numerical analysis. Polytechnic University of Catalonia - University of Genoa, PhD disseration
49. Ferrero C, Rossi M, Roca P, Calderini C (2021). Experimental and numerical analysis of a scaled dry-joint arch on moving supports. Int J Masonry Res Innov 6(4).
50. Portioli FPA, Cascini L (2017) Large displacement analysis of dry-jointed masonry structures subjected to settlements using rigid block modelling. Eng Struct 148(2):485–496
51. Smars P (2010) Kinematic stability of masonry arches. Adv Mater Res 133:429–434
52. Como M (2016). Statics of historic masonry constructions, Springer International Publishing Switzerland